Supporting Information for "Observed regional impacts of marine heatwaves on sea-air CO_2 exchange"

Catherine Li[1,2], Friedrich A. Burger[1,2], Christoph C. Raible[1,2] and Thomas L. Frölicher[1,2]

[1]Climate and Environmental Physics, Physics Institute, University of Bern, Bern, Switzerland.

[2]Oeschger Centre for Climate Change Research, University of Bern, Bern, Switzerland.

Contents of this file

Corresponding author: Thomas L. Frölicher, Climate and Environmental Physics, Physics Institute, University of Bern, Bern, Switzerland. (thomas.froelicher@unibe.ch)

Table S1: Summary of the six observation-based pCO_2 products used in SeaFlux.

pCO_2 mapping product	Area coverage (% global ocean)	Surface-ocean pCO_2 data	Reference
CMEMS-FFNN	89%	SOCAT v5	Denvil-Sommer et al. (2019) Chau et al. (2022)
CSIR-ML6	93%	SOCAT v5	Gregor et al. (2019)
JENA-MLS	100%	SOCAT v1.5	Rödenbeck et al. (2013)
JMA-MLR	85%	SOCAT v5	Iida et al. (2020)
MPI-SOMFFN	89%	SOCAT v5	? (?) ? (?)
NIES-FNN	91%	SOCAT v2	Zeng et al. (2014)

Table S2: Summary of the five observation-based wind products used in combination with the observation-based pCO_2 products in SeaFlux. Mean wind speed is given for the ice-free ocean for the period 1990 to 2019.

Wind product name	Temporal Resolution (hr)	Spatial Resolution (°)	Date range	Mean speed (m s^{-1})	Scaling (a)	Reference
Cross-Calibrated Multi-Platform v2	6	0.25	1988-present	7.7	0.257	Atlas et al. (2011)
ECMWF Reanalysis 5th Generation	1	0.25	1979-present	7.5	0.271	Hersbach et al. (2020)
Japanese 55-year Reanalysis	3	0.50	1958-present	7.6	0.260	Kobayashi et al. (2015)
NCEP-NCAR reanalysis 1	6	2.50	1948-present	7.2	0.287	Kalnay et al. (1996)
NCEP-NCAR reanalysis 2	6	2.50	1979-present	8.3	0.218	Kanamitsu et al. (2002)

Table S3: Definition of regional latitude–longitude boxes.

Region	Longitude range	Latitude range
Subpolar Northern Pacific	140°E - 130°W	65°N - 40°N
Subpolar Northern Atlantic	70°W - 10°E	65°N - 40°N
Low-to-mid Latitude Northern Hemisphere	Full	10°N - 40°N
Equatorial Indian	40°E - 125°E	10°S - 10°N
Equatorial Pacific	125°E - 80°W	10°S - 10°N
Equatorial Atlantic	77°W - 10°E	10°S - 10°N
Low-to-mid Latitude Southern Hemisphere	Full	10°S - 45°S
Southern Ocean	Full	65°S - 45°S

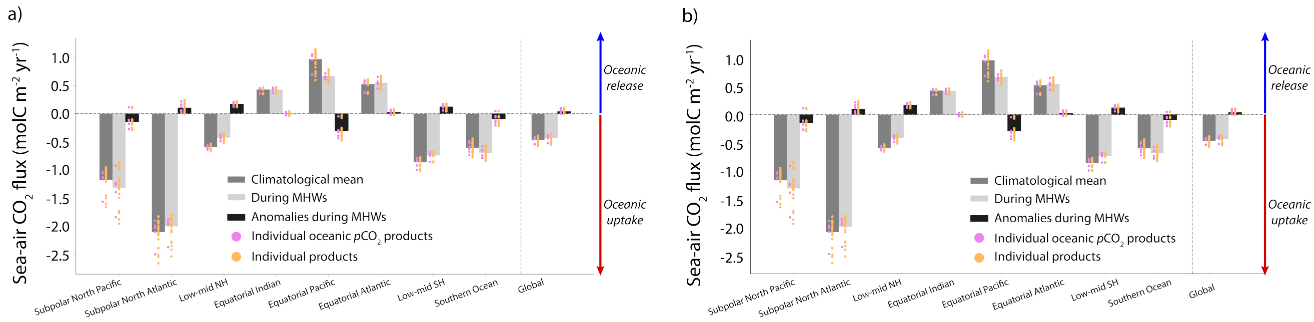

Figure S1: Climatological mean sea-air CO_2 flux, mean sea-air CO_2 flux during MHWs and mean sea-air CO_2 flux anomalies during MHWs for the years 1990-2019, when MHWs are calculated using the period (a) 1982-2021 and b) 1990-2019. Panel a is similar to Figure 1b of the main text.

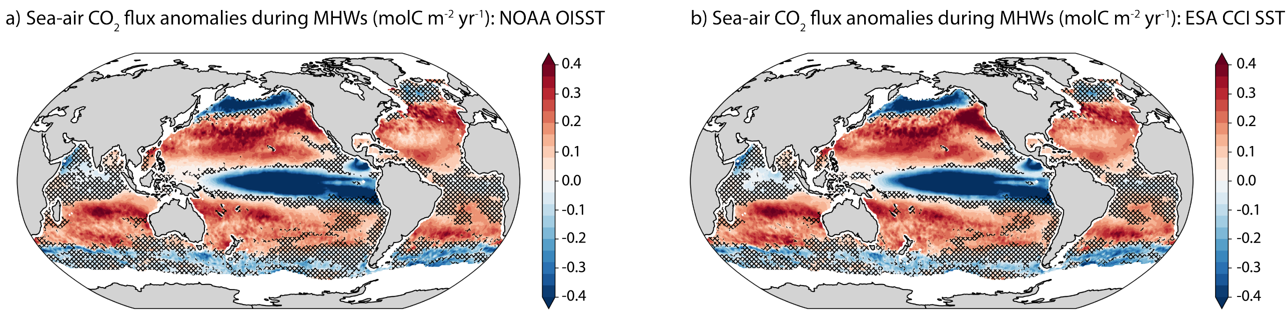

Figure S2: Observation-based sea-air CO_2 flux anomalies during MHWs averaged over the 1990-2019 period and across all observation-based CO_2 flux products. MHWs are defined using the (a) NOAA OISST and the (b) ESA CCI SST product, respectively. Data is only shown for regions where all six observation-based pCO_2 products have data. Hatching indicates regions, where the anomalies are not statistically different (5% level using a two-sampled t-test).

References

Atlas, R., Hoffman, R. N., Ardizzone, J., Leidner, M., Jusem, J. C., Smit, D. K., & Gombos, D. (2011). Cross-calibrated, multiplatform ocean surface wind velocity product for meteorological and oceanographic applications. *Journal of Climate*, 157–174. doi: https://doi.org/10.1029/2019JC015367

Chau, T. T. T., Gehlen, M., & Chevallier, F. (2022). A seamless ensemble-based reconstruction of surface ocean $p\mathrm{CO}_2$ and air-sea CO_2 fluxes over the global coastal and open oceans. *Biogeosciences*, *19*, 1087–1109. doi: https://doi.org/10.5194/bg-19-1087-2022

Denvil-Sommer, A., Gehlen, M., Vrac, M., & Mejia, C. (2019). LSCE-FFNN-v1: A two-step neural network model for the reconstruction of surface ocean $p\mathrm{CO}_2$ over the global ocean. *Geoscientific Model Development*, *12*(5), 2091-2105. doi: https://doi.org/10.5194/gmd-12-2091-2019

Gregor, L., & Gruber, N. (2021). Oceansoda-ethz: a global gridded data set of the surface ocean carbonate system for seasonal to decadal studies of ocean acidification. *Earth System Science Data*, *13*(2), 777–808. doi: 10.5194/essd-13-777-2021

Gregor, L., Lebehot, A. D., Kok, S., & Scheel Monteiro, P. M. (2019). A comparative assessment of the uncertainties of global surface ocean CO_2 estimates using a machine-learning ensemble (CSIR-ML6 version 2019a) – have we hit the wall? *Geoscientific Model Development*, *12*, 5113–5136. doi: https://doi.org/10.5194/gmd-12-5113-2019

Hersbach, H., Bell, B., Berrisford, P., Hirahara, S., Horányi, A., Muñoz-Sabater, J., . . . Thépaut, J.-N. (2020). The ERA5 global reanalysis. *Quarterly Journal of the Royal Meteorological Society*, *146*, 1999–2049. doi: https://doi.org/10.1002/qj.3803

Iida, Y., Takatani, Y., Kojima, A., & Ishii, M. (2020). Global trends of ocean CO_2 sink and ocean acidifcation: an observation-based reconstruction of surface ocean inorganic carbon variables. *Journal of Oceanography*, *77*, 323–358. doi: https://doi.org/10.1007/s10872-020-00571-5

Kalnay, E., Kanamitsu, M., Kistler, R., Collins, W., Deaven, D., Gandin, L., … Joseph, D. (1996). The NCEP/NCAR 40-year reanalysis project. *Bulletin of the American Meteorological Society*, *77*, 437–472. doi: https://doi.org/10.1175/1520-0477(1996)077⟨0437:TNYRP⟩2.0.CO;2

Kanamitsu, M., Ebisuzaki, W., Woollen, J., Yang, S.-K., Hnilo, J. J., Fiorino, M., & Potter, G. L. (2002). NCEP–DOE AMIP-II reanalysis. *Bulletin of the American Meteorological Society*, *83*, 1631–1644. doi: https://doi.org/10.1175/BAMS-83-11-1631

Kobayashi, S., Ota, Y., Harada, Y., Ebita, A., Moriya, M., Onoda, H., … Takahasi, K. (2015). The JRA-55 reanalysis: General specifications and basic characteristics. *Journal of the Meteorological Society of Japan*, *93*, 5–48. doi: https://doi.org/10.2151/jmsj.2015-001

Le Grix, N., Zscheischler, J., Laufkötter, C., Rousseaux, C. S., & Frölicher, T. L. (2021). Compound high-temperature and low-chlorophyll extremes in the ocean over the satellite period. *Biogeosciences*, *18*(6), 2119–2137. doi: https://doi.org/10.5194/bg-18-2119-2021

Rödenbeck, C., Keeling, R. F., Bakker, D. C. E., Metzl, N., Olsen, A., Sabine, C., & Heimann, M. (2013). Global surface-ocean pCO_2 and sea–air CO_2 flux variability from an observation-driven ocean mixed-layer scheme. *Ocean Science*, *9*, 193–216. doi: https://doi.org/10.5194/os-9-193-2013

Zeng, J., Nojiri, Y., Landschützer, P., Telszewski, M., & Nakaoka, S.-i. (2014). A global surface ocean fCO_2 climatology based on a feed-forward neural network. *Journal of Atmospheric and Oceanic Technology*, *31*(8), 1838-1849. doi: https://doi.org/10.1175/JTECH-D-13-00137.1

Zscheischler, J., & Seneviratne, S. I. (2017). Dependence of drivers affects risks associated with compound events. *Science Advances*, *3*(6), e1700263. doi: 10.1126/sciadv.1700263

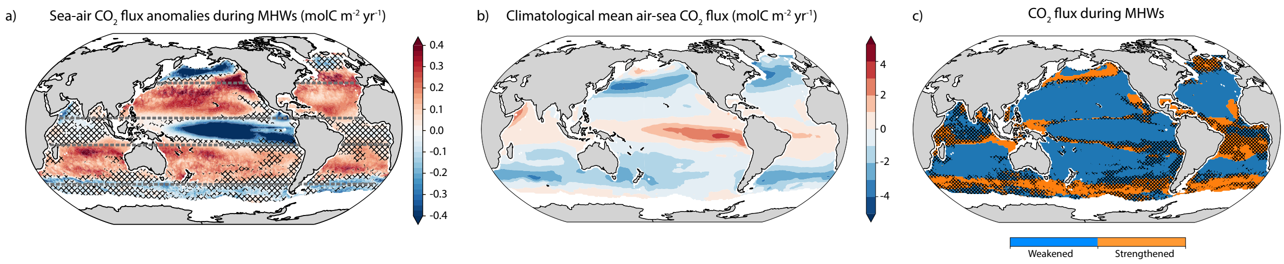

Figure S3: a) Observation-based sea-air CO_2 flux anomalies during MHWs and b) climatological sea-air CO_2 flux averaged over the 1990-2019 period and across all observation-based products. Data is only shown for regions where all six observation-based pCO$_2$ products have data. c) Map indicating where the sea-air CO_2 flux is weakened (blue) or strengthened (orange) during MHWs over the 1990-2019 period and across all observation-based products. Hatching in (a) and (c) indicate regions, where the anomalies are not statistically different (5% level using a two-sampled t-test).

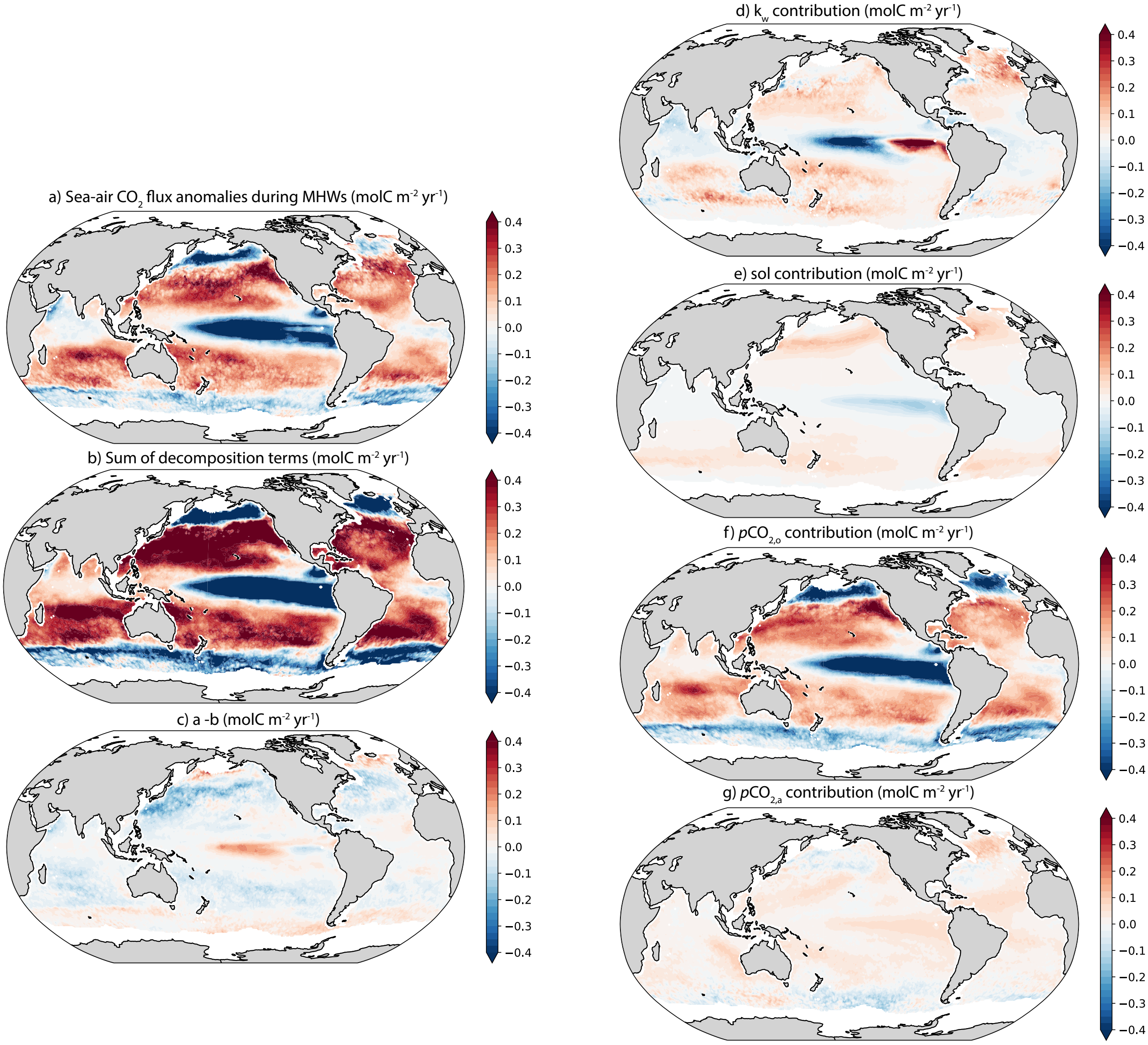

Figure S4: Global maps of the Taylor decomposition of the sea-air CO_2 flux anomalies during MHWs over the 1990-2019 period averaged across all observation-based products. The left hand column shows the sea-air CO_2 flux anomalies during MHWs (top), the sum of the flux decomposition contributions (middle), and the difference between the two (bottom). The right hand column shows the contributions of each flux component (k_w, solubility, $p\mathrm{CO}_{2,o}$ and $p\mathrm{CO}_{2,a}$) to the sea-air CO_2 flux anomaly during MHWs.

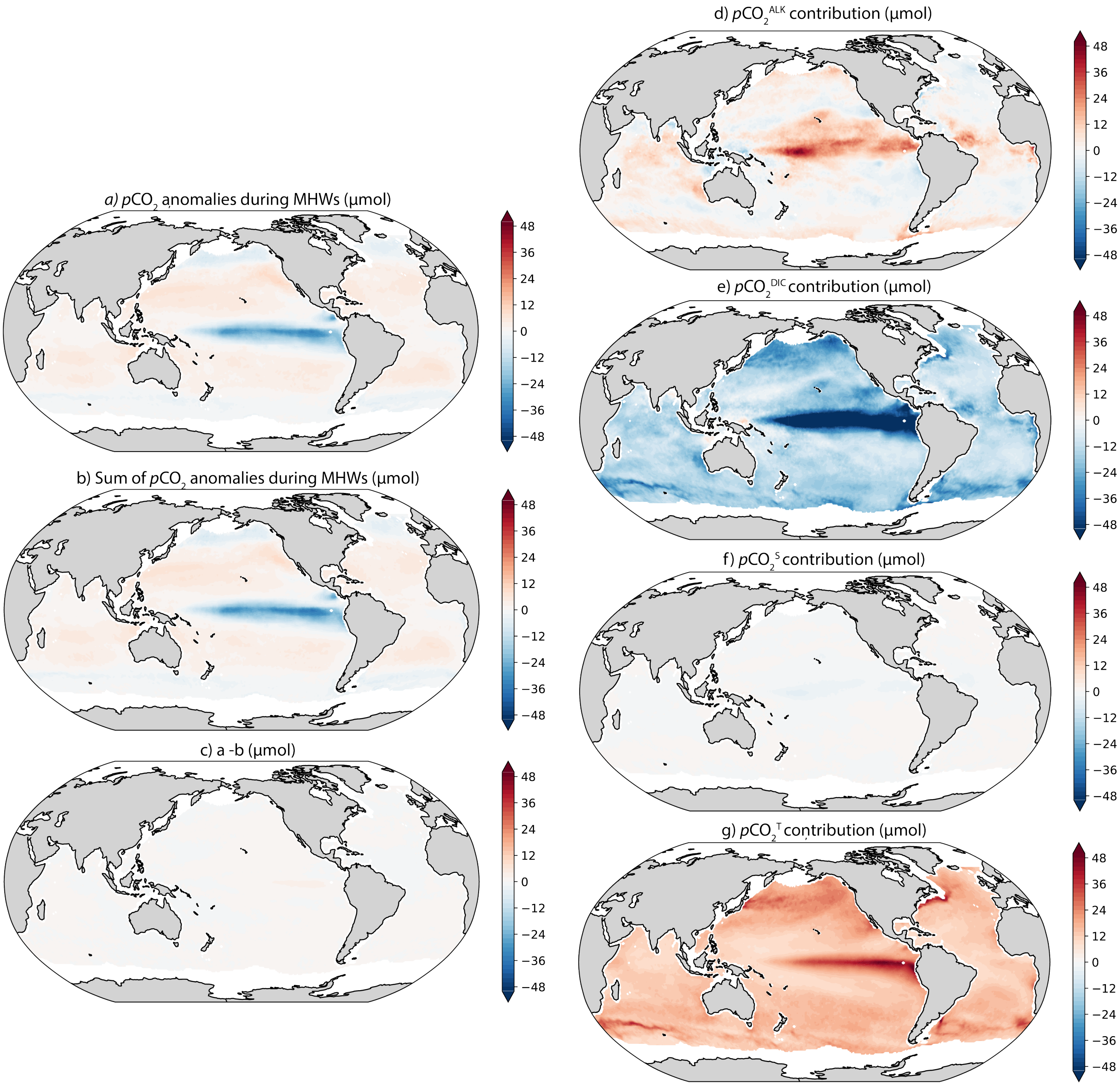

Figure S5: Global map of the Tayler decomposition of the $pCO_{2,o}$ anomalies during MHWs averaged over the 1990-2019 period and across all observation-based products. The left hand column shows the $pCO_{2,o}$ anomalies during MHWs (top), the sum of the $pCO_{2,o}$ decomposition terms (middle), and the difference between the two (bottom). The right hand column shows the contributions of each $pCO_{2,o}$ component (alkalinity, dissolved inorganic carbon, salinity, and temperature) to the $pCO_{2,o}$ anomalies during MHWs.

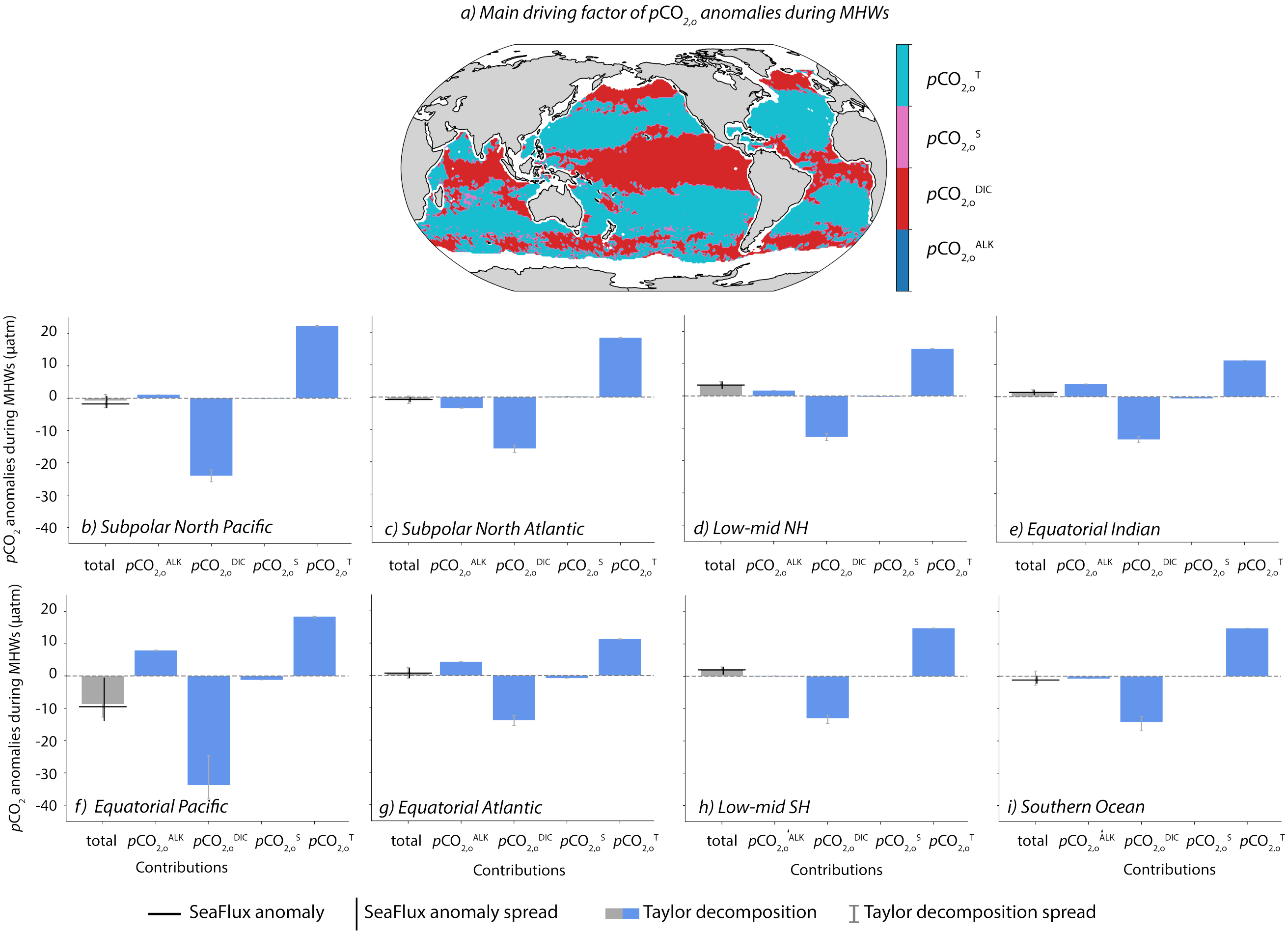

Figure S6: Same as Figure 3 in the main text, but using the OceanSODA-ETHZ Alkalinity data from Gregor and Gruber (2021) instead of the alkalinity data based on LIARv2.

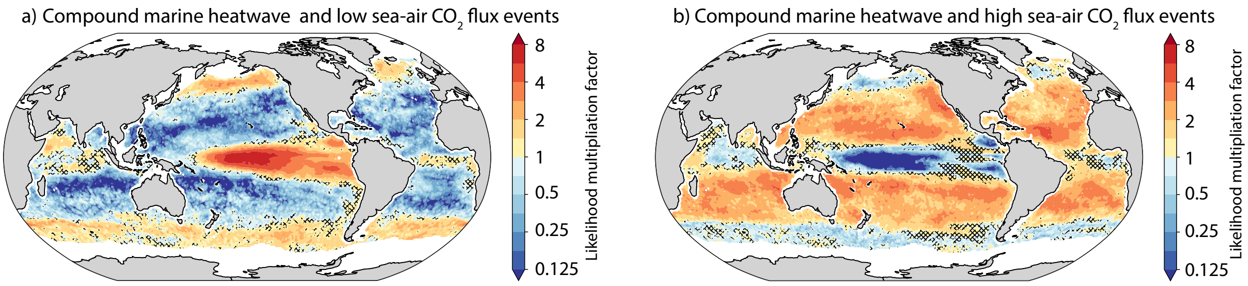

Figure S7: Observation-based product ensemble-mean likelihood multiplication factor (LMF) for (a) compound MHWs and low sea-air CO_2 flux events and (b) for MHWs and high sea-air CO_2 flux events. The LMF is a metric commonly used in compound event studies to describe how many times more or less likely compound events are compared to their expected frequency under the assumption of independence (Zscheischler & Seneviratne, 2017; Le Grix et al., 2021). Warm colors (LMF $>$ 1) indicate that MHWs and low/high sea-air CO_2 flux events co-occur more frequently than by chance, while cold colors (LMF $<$ 1) indicate suppressed co-occurrence. Ocean regions where LMF is not significantly different from 1 (i.e., where the product ensemble-mean LMF is not significantly different from 1 based on a one-sample t-test) are hatched.